The International Journal of Robotics Research

Design of a Hollow Hexaform Torque Sensor for Robot Joints

Farhad Aghili, Martin Buehler and John M. Hollerbach

The online version of this article can be found at:

Published by:

SAGE Publications

http://www.sagepublications.com

On behalf of:

M

Multimedia Archives

Additional services and information for **The International Journal of Robotics Research** can be found at:

Email Alerts: http://ijr.sagepub.com/cgi/alerts

Subscriptions: http://ijr.sagepub.com/subscriptions

Reprints: http://www.sagepub.com/journalsReprints.nav

Permissions: http://www.sagepub.com/journalsPermissions.nav

Citations (this article cites 10 articles hosted on the
SAGE Journals Online and HighWire Press platforms):
http://ijr.sagepub.com/cgi/content/refs/20/12/967

Farhad Aghili

Canadian Space Agency
Saint-Hubert, Québec, J3Y 8Y8
Farhad.Aghili@space.gc.ca

Martin Buehler

Department of Mechanical Engineering
McGill University
Montreal, Quebec, Canada H3A 2A7
buehler@cim.mcgill.ca

John M. Hollerbach

Department of Computer Science
University of Utah
Salt Lake City, UT 84112, USA
jmh@cs.utah.edu

Design of a Hollow Hexaform Torque Sensor for Robot Joints

Abstract

This work describes the design of a new one-axis torque sensor. It achieves the conflicting requirements of high stiffness for all six force and torque components, high sensitivity for the one driving torque of interest, and yet very low sensitivity for the other five force/torque components. These properties, combined with its donut shape and small size, make this sensor an ideal choice for direct-drive robotic applications. Experimental data validate the basic design ideas underlying the sensor's geometry, the finite element model used in its optimization, and the advertised performance.

KEY WORDS—torque sensor, robot joint, joint torque control

1. Introduction

The benefits of using joint torque sensory feedback to improve the performance of robotic systems have been recognized in the robotics community (Asada and Youcef-Toumi 1987; Stokic and Vukobratovic 1993; Hashimoto, Kiyosawa, and Paul 1993; Kosuge, Takeuchi, and Furuta 1990; Aghili, Buehler, and Hollerbach 1998a, 2001). For example, joint torque feedback can be used to compensate the nonlinearities and modeling uncertainties of manipulator dynamics (Aghili, Buehler, and Hollerbach 1997, 2001; Kosuge, Takeuchi, and Furuta 1990; Hashimoto 1989) or simply those of actuators (Asada and Lim 1985; deSilva, Price, and Kanade 1987;

Zhang and Furusho 1998; Luh, Fisher, and Paul 1983). Moreover, in geared systems, the implementation of model-based controllers is difficult without measuring the actual output torque since the efficiency of gears depends greatly on the torque and, to a lesser extent, on the joint velocity, and yet these data are typically not made available by gear manufacturers. Thus, there is a need for torque sensors that can be integrated simply between the actuator (and possibly gear) and the load. The sensor research described in this paper was motivated by the lack of suitable sensors needed for our joint servo system (Aghili, Buehler, and Hollerbach 2000).

Accurate joint torque measurement encounters several design challenges. In the design of robot manipulators, it is desirable that much of the torque/force reaction of the link load on the joints appears in the form of nontorsional components because actuation then takes less effort. SCARA robot arm designs, for instance, prevent gravity torques from acting on the joint motors (Newman and Patel 1991). However, since torque sensors are directly attached to the motor's distal links, they have to bear those potentially large nontorsional components. The first challenge is to measure torque with minimal influence from simultaneous and potentially large nontorsional components. In the sequel, we shall call the one axis of the motor torque of interest the *torsion*. For simplicity, we shall call the other two torque and three force components the *nontorsional components*. The second challenge relates to the sensor stiffness. High torsion stiffness is important because any deflection adds positioning errors that cannot be compensated by the joint servo controller. To increase the signal-to-noise (S/N) ratio and sensitivity of the sensor, it is

967

desirable to design a structure that generates a large strain for a given load torque. However, the sensitivity introduces a torsion compliance that must be minimized. Thus, there are two conflicting requirements: high stiffness and high sensitivity for torsion. A solution to these two challenges will be described in this paper and is new compared to existing designs. Some aspects of this research have been previously reported in Aghili, Buehler, and Hollerbach (1997b, 1998b).

There is a large literature on the systematic design of six-degree-of-freedom (DOF) force/torque sensors (Hirose and Yoneda 1990; Svinin and Uchiyama 1995; Uchiyama, Bayo, and Palma-Villalon 1991). It is important to note that the design criteria for one- and six-DOF sensors are very different. For instance, isotropy (uniform sensitivity) is a desirable property of a six-DOF force/torque sensor, and hence its elastic structure tends to be fragile and compliant in all directions. In contrast, the elastic sensitivity of a torque sensor has to be maximized only around its torsional axis.

Various techniques have been proposed to instrument geared motors for torque sensing (Hashimoto, Kiyosawa, and Paul 1993; Luh, Fisher, and Paul 1983; Pfeffer, Khatib, and Hake 1989; Vischer and Khatib 1990), while little attention has been paid to find an adequate structure for joint torque sensing (Asada and Lim 1985; Jacobsen et al. 1991; deSilva, Price, and Kanade 1987). Hashimoto, Kiyosawa, and Paul (1993) used the elasticity of the flex-spline in a harmonic drive to measure the joint torque. This technique has the advantage of using the existing structural flexibility of the robots. However, eliminating the error caused by rotation of the wave generator is difficult because it requires a nontrivial gear modification, and this approach cannot be used in direct-drive systems. Many researchers (Pfeffer, Khatib, and Hake 1989; Wu 1985; Luh, Fisher, and Paul 1983; deSilva, Price, and Kanade 1987; Asada and Lim 1985; Vischer and Khatib 1995) have chosen not to place the sensor directly at the joint shaft to avoid the detrimental effects of the support forces and moments. Pfeffer, Khatib, and Hake (1989) replaced standard attachment bolts in the PUMA 500 joints with a flexure instrumented with strain gauges. Wu (1985) used a shaft with a thin hollow circular section that was supported by two bearings. Strain gauges were mounted on the thin section. Luh, Fisher, and Paul (1983) cemented stain gauges on the connecting output shaft, which was mounted to the flex-spline of the harmonic drive for each joint of the Stanford manipulator. Visher and Khatib (1995) integrated a torque sensor with the gear transmission, while Asada and Lim (1985) and Asada and Youcef-Toumi (1987) integrated strain gauges in the hub supporting the robot of a direct-drive motor. The strain gauges were cemented on three beams connecting the outer ring, mounted to the motor rotor, and the inner ring, which was coupled to the motor shaft. Asada and Lim cemented strain gauges inside the rotor of a direct-drive motor for torque measurement. Since these sensors were not mounted directly on the joints of a manipulator, the entire set of forces and moments were supported by the bearing set rather than the sensor structure. However, these sensors were not ideal because they could not account for the friction in the joint bearings. Moreover, the mechanical joints were complicated and sometimes bulky. In commercial torque sensors (AMTI 1996; Himmelstein and Company 1991; Lebow 1997), nontorsional components are not permitted or are highly restricted. Furthermore, they usually come in bulky packages, are built for shaft mounting, and thus are not suitable for integration in a robot joint.

Figure 1 illustrates conventional geometries (A, B, C, and D) and the proposed hollow hexaform design (E) for torque sensors. Solid (A) and hollow (B) cylinders have been used extensively for joint torque sensing (Pfeffer, Khatib, and Hake 1989; Wu 1985; Luh, Fisher, and Paul 1983; deSilva, Price, and Kanade 1987; Wu and Paul 1980) but are sensitive to nontorsional components (Wu and Paul 1980). For this reason, they are usually mounted before the joint bearings so that the bearing can support the nontorsional components. In addition to requiring a bearing support structure, the main drawback of this method is that joint friction cannot be observed by the sensor. Hub-sprocket designs (C) have been used for geared joints (Hirzinger et al. 1994, 2001; Vischer and Khatib 1995) as well as direct-drive joints (Asada and Lim 1985; Asada and Youcef-Toumi 1987; Tani, Hatamura, and Nagao 1983). Although a better rejection to nontorsional components has been reported for this type of sensor (Vischer and Khatib 1995), the structure is not adequate for a modular robot joint. This is because of the drastic change in the physical size between the input (inner ring) and output (outer ring) of the sensor. Rather, this type of sensor should be integrated with the gear or with the rotor of a direct-drive motor, and hence it suffers from the same drawbacks as type (A) and (B) sensors.

The hollow cruciform design (D) is used in commercially available torque sensors (Lebow 1997) and has been analyzed in Joo, Lee, and Kang (1998). In this design, strain is induced mainly by bending of the wing elements. To achieve good sensitivity, the wing and sensor height is large, and as a result, the stiffness is low and nontorsional torques must be kept small. The proposed hollow hexaform sensor (E), described in this paper, is similar in its basic geometry to the hollow cruciform sensor (D) with only four wings. However, there are fundamental functional differences. Due to the increased number of wing pairs and the shorter height, strain is induced primarily in torsion, resulting in a much stiffer sensor and improved sensitivity. In addition, this design can be optimized to support nontorsional torques, making it suitable for direct-drive robotic applications.

This paper is arranged as follows. In Section 2, the general conditions are proposed on the mechanical design and the location of the strain gauges so that the Wheatstone bridge decouples the joint torque output signal from the nontorsional components. Additional design issues, such as torsional strain sensitivity, torsional stiffness, the sensor shape, and material, are discussed as well. Section 3 describes the detailed sensor
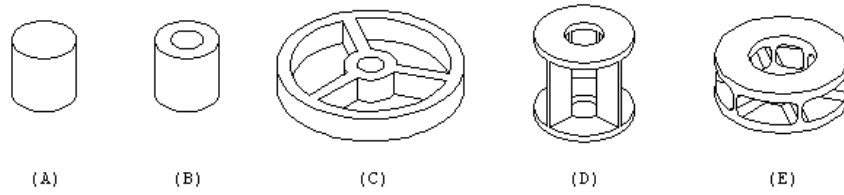
Fig. 1. Different structure for torque sensor: (A) solid cylinder, (B) hollow cylinder, (C) hub-sprocket, (D) hollow cruciform, and (E) new hollow hexaform design.

design and how the finite element method (FEM) was used to optimize the sensor geometry. Experimental validation of the sensor's characteristics is presented in Section 4.

2. Sensor Design

In this section, we describe how the new hollow hexaform sensor achieves

1. high sensitivity to torsion,

2. low sensitivity to nontorsional components, and

3. high stiffness in all axes of forces and moment.

2.1. Design for Decoupling

In general, torque measurements are derived from strain measurements at several locations on an elastic sensor body. Assuming a linearly elastic material, there is a linear relationship between the applied forces and torques and the resultant strains described by

$$\boldsymbol{\epsilon} = \mathbf{C}\,\mathbf{f}, \qquad (1)$$

where $\boldsymbol{\epsilon} = [\epsilon_1, \epsilon_2, \cdots, \epsilon_n]^T$ is the vector of n measured strains, $\mathbf{f} = [f_x, f_y, f_z, n_x, n_y, n_z]^T \in \mathbb{R}^6$ is the generalized force/moment vector acting at the center of the sensor body where the z-axis and joint axis are identical, and $\mathbf{C} \in \mathbb{R}^{n \times 6}$ is the sensitivity matrix whose elements $[c_{ij}]$ denote the sensitivity of the ith strain gauge to the jth component of the generalized force/moment. This matrix permits the reconstruction of the torsion moment from the output signal with the gain vector. Unlike in 6-axis force/torque sensors, it is desired to reconstruct only the torsion moment n_z from the measured strains $\boldsymbol{\epsilon}$. However, the sensitivity matrix underlies the mechanical coupling transmitted through the force/moment sensor structure. Therefore, the sensor output should be decoupled from the nontorsional components of forces and moments. We show that one can use the additive properties of the Wheatstone bridge to achieve the decoupling without the need for any subsequent arithmetic. The resulting advantage is a reduction of instrumentation and the number of wires by completing the bridge wiring inside the sensor, as well as a simplification of tedious calibration.

The question arises concerning the condition for which there exists such a mapping. It is necessary to consider each component of force to be a linear function of all stain gauge sensors to correct for the coupling. Let v_o and v_{ex} represent the output voltage and the excitation voltage of a half-bridge configuration, and let GF denote the gauge factor (Omega 1995) of the strain gauges. Then, assuming every strain gauge pair constitutes a half-bridge circuit, the overall voltage output is given by

$$v_o = \alpha_e \mathbf{v}^T \boldsymbol{\epsilon}, \qquad (2)$$

where $\alpha_e = 0.5 GF v_{ex}$ is the gain of the strain gauges, and $\mathbf{v} = [-1, 1, -1, 1, \cdots]^T$ represents the gain signs corresponding to the negative and positive branches of a Wheatstone bridge circuit. Substituting $\boldsymbol{\epsilon}$ from eq. (1) into eq. (2), we have

$$v_o = \alpha_e \left(\mathbf{C}^T \mathbf{v}\right)^T \mathbf{f}. \qquad (3)$$

It is evident from eq. (3) that, in the most general case, the sensor output is the superposition of weighted components of the generalized forces and moments transmitted through the sensor unless all weights related to the exogenous forces moments are zero. That is,

$$\mathbf{C}^T \mathbf{v} = \alpha_m \mathbf{e}, \qquad (4)$$

where $\mathbf{e} = [0, 0, 0, 0, 0, 1]^T$, and α_m is the (scalar) mechanical gain of the sensor. In this case, the sensor output is solely proportional to the torsion torque; that is,

$$v_o = \alpha n_z, \qquad (5)$$

where $\alpha = \alpha_e \alpha_m$ represents the overall sensitivity of the sensor. Eq. (4) underlines a condition on the structure of a torque sensor by which the sensor exhibits the decoupling. As a result, such as sensor is not sensitive to the supporting forces and moments transmitted through the structure of the sensor.

For the candidate geometry in Figure 2 and with four strain gauges located on the numbered locations, the parametric form of the sensitivity matrix can be derived from the symmetry of the structure with respect to the external forces and torques as
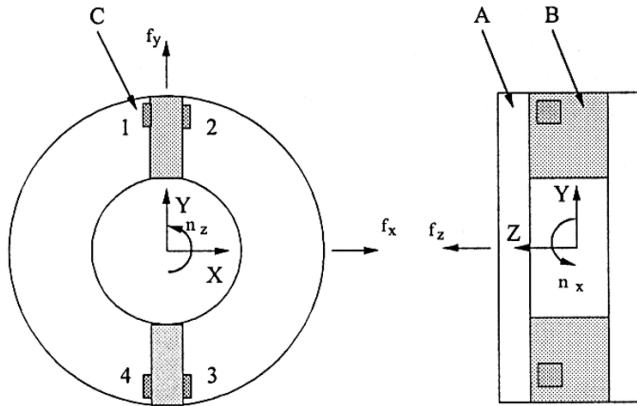
Fig. 2. Basic torque sensor structure. (A) solid disks, (B) elastic element, and (C) strain gauge.

$$\mathbf{C} = \begin{bmatrix} c_{11} & c_{12} & c_{13} & c_{14} & c_{15} & -c_{16} \\ c_{21} & c_{12} & c_{13} & c_{14} & -c_{15} & c_{16} \\ c_{21} & c_{32} & c_{13} & -c_{14} & -c_{15} & -c_{16} \\ c_{11} & c_{32} & c_{13} & -c_{14} & c_{15} & c_{16} \end{bmatrix}.$$

The jth column of the matrix represents the strain sensitivities in the four site locations with respect to the jth load case (e.g., the third column represents the sensitivity due to f_z). The identical elements in the matrix can be implied from the symmetric configuration of the structure with respect to different load cases. For instance, the symmetric condition of the stain gauges with respect to the axial load, f_z, implies identical elements of the third column. Now one can readily show that $\mathbf{C}^T \mathbf{v} = 4c_{16}\mathbf{e}$, and hence the structure satisfies the condition (4) for mechanical decoupling.

There are two main reasons in practice that violate the above assumption of exact symmetry among the measured strains. First, strain gauges exhibit variations in their gauge factor. Second, the strain gauges will be placed on areas with high strain gradients. This makes the gauge outputs sensitive to placement errors. This can also be modeled as a gauge gain error. As a consequence, exact cancellation of the nontorsional components may not be achieved with the theoretical gain vector. By virtue of the linear mapping (1), the nontorsional components produce no output if all elements of the sensitivity matrix except that for the last column are sufficiently small. This implies that the strain sensitivity to the nontorsional components has to be held to a minimum by mechanical design. This condition, in conjunction with the decoupling property of the sensitivity matrix, actually determines the capability of the sensor to reject the effect of nontorsional force/torque to the output and provide a high fidelity output signal.

2.2. Maximum Sensitivity

To increase the S/N ratio and the resolution of the sensor, it is desirable to design the elastic component to provide large output signals (i.e., large mechanical gain α_m). Therefore, one of the design criteria is to increase the torsional sensitivity, subject to not exceeding the allowable strain. In the absence of nontorsional components, the maximum attainable strain sensitivity depends solely on the material properties as the strain due to the maximum load should be close to the maximum allowable material strain or stress. However, nontorsional components produce strains that add to the strain caused by torsion. To ensure that the allowable maximum material strain is not exceeded, we consider the worst-case scenario where the generalized force/torque vector has its maximum force and moment. Then, to exploit maximum torsion sensitivity, c_{16}, the other sensitivity components (i.e., $\{c_{11}, \cdots, c_{15}\}$) must be minimized by proper geometry design. This design requirement is consistent with a decoupling property of the sensor. It is interesting to note that cylinders are mainly used in the design of commercial torque sensors. By elementary strength of material analysis, one can show that bending moments produce twice the stress than the same magnitude torsion moment. This is why shear and thrust forces and bending moments must be kept small in these sensors.

2.3. High Torsional and Bending Stiffness

Torsional deflection degrades the position accuracy of the joint angle controller. Moreover, increasing the S/N ratio requires maximizing the sensor sensitivity. However, highly stiff sensors tend to be less sensitive. Therefore, one of the critical design challenges is to maximize the stiffness while maintaining high sensitivity. We propose γ, called *structure efficiency*, which is the product of sensitivity and stiffness as a performance index to capture these contradictory requirements:

$$\gamma \triangleq (\text{torsional sensitivity}) \cdot (\text{torsional stiffness})$$

$$= \frac{4\alpha_e \epsilon}{n_z} \cdot \frac{n_z}{\delta} = 4\alpha_e \frac{\epsilon}{\delta}, \tag{6}$$

where δ is the torsional deflection. As mentioned earlier, the gain of the strain gauge, α_e, is independent of sensor structure. Moreover, ϵ/δ is a dimensionless variable that captures the ratio of the local and global strains. These facts suggest that γ is a decisive factor in the sensor design and should be maximized. Moreover, since it is dimensionless, the index is a useful base for comparison of different-size torque sensors. The index is maximized in elastic structures that produce high strain concentration in torsion. In theory, there is no limit on the strain concentration in an elastic body. However, the high strain concentration takes place in a very small area, which might be smaller than the physical size of available strain gauges. Moreover, since strain gauges average the strain field

over their area, the detected strain can be significantly lower than the calculated value. Therefore, it is important to generate high strain over a sufficiently large area. This objective seems difficult to formulate analytically but can be inspected by FEM.

Introducing a torque sensor in a robot joint adds flexibility. Although torsional flexibility can, in principle, be compensated via sophisticated controllers, deflection in the other axes is more problematic. Consequently, another design criterion dictates high stiffness in nontorsional directions. Fortunately, the requirements for low deflection and low strain sensitivity for nontorsional components are consistent. The structure shown in Figure 2 exhibits high bending stiffness around the x-axis. However, its poor stiffness around the y-axis is a drawback. This problem can be simply solved by adding more wing pairs, as shown in Figure 3. This improves the uniformity of the bending stiffness along different axes as well as the body stiffness. In general, all performance aspects of the sensor improve with the number of wing pairs, but since we will want to machine the sensor from one solid piece of metal, the limit is imposed by manufacturability. For this reason, we consider six wings in our design.

2.4. Practical Shape Considerations

Addition of a torque sensor to a robot joint must not require the redesign of the joint and should result in a minimal change in the manipulator's kinematics, particularly the link offset. Hence, a shape with a small width is desirable. Minimizing the effects of thermal stresses is a design factor that cannot be ignored. Motors are a source of heat that flows from the motor to the attached link through the sensor body. Therefore, it is desirable to have an axis-symmetric design that constrains the heat to flow in the axial direction, where no position constraint usually exists. The common hub-sprocket designs are prone to thermal stresses because of the temperature difference between the hub and the wheel. Since the sensor is specifically designed for a direct-drive motor with hollow shaft, flange mounting is preferred. Finally, the body
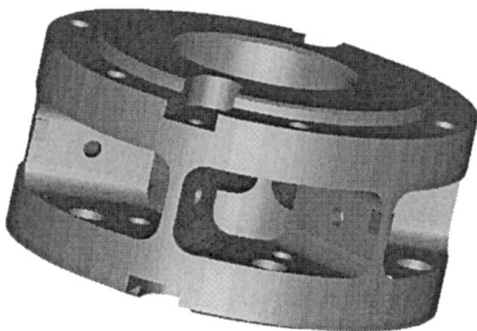
should be designed for ease of manufacture. It should be a *monolithic structure*; that is, the body should be machined from a solid piece of metal. This decreases the hysteresis and increases the strength and repeatability of the sensor. The hollow hexaform geometry shown in Figure 3 satisfies these requirements.

2.5. Material Properties and Overloading

So far, only geometric properties of the elastic body have been considered. Nevertheless, the stiffness and sensitivity characteristics of the torque sensor are also determined by the material properties. The maximum allowable strain for foil strain gauges is typically 3%, which is at least one order of magnitude higher than that of industrial metals ϵ_a, making the materials the limiting factor for sensitivity. Furthermore, the stiffness depends linearly on Young's modulus E of the material. By virtue of Hook's law,

$$\sigma_a = E \, \epsilon_a,$$

one can conclude that high sensitivity and stiffness are achievable simultaneously only by use of a high-strength material.

Because a linear response is desired from the sensor, the chosen sensor material must have a linear strain-stress relationship. Steel is the best available industrial material that has good linearity properties within a large stress range. Moreover, due to the oscillatory nature of the loading, steel can work with infinite fatigue life (Shigley 1989) as the allowable strains are determined based on the endurance limit. The endurance limit or fatigue limit is the maximum stress under which mechanical failure will not occur, independent of the number of load cycles. Only ferrous metals and alloys have an endurance limit.

The sensor is designed for a nominal torque of 300 Nm, which is based on the endurance limit of mild steel and is twice as much as the yield point. Hence, the safety factor in torque overloading is two. Remarkably, FEM results demonstrated that the stress induced by the bending moment is very low for the proposed structure. As a result, the structure can resist bending moments as high as 2000 Nm, which is almost an order of magnitude higher than the nominal torque.

2.6. Thermal Deviation

The gauge resistance and gauge factor of all known strain-sensitive materials vary with temperature. The change in resistance with temperature for a mounted strain gauge is a function of the difference in the thermal expansion coefficient between the gauge and the sensor body and of the thermal coefficient of resistance of the gauge alloy. Self-temperature compensating gauges can be achieved for specific materials by processing the strain-sensitive alloy such that it has thermal characteristics that compensate for the effects of the mismatch in thermal expansion coefficients between the gauge and the

Fig. 3. Elastic structure of the torque sensor.

body of the sensor (Omega 1995). The manufacturer of the strain gauge (Omega 1995) claims that its products accurately compensate the effect of temperature if they are chosen according to a specific coefficient of thermal expansion of material on which the gauges are mounted.

3. FEM Design and Analysis

Once we had determined the basic hollow hexaform shape of the sensor, we used the FEM capabilities of IDEAS (Structural Dynamics Research Corp.) to optimize the sensor dimensions and determine the size and placement of the strain gauges. Strain concentration is the design key to simultaneously achieve high torsional sensitivity and high stiffness. For maximum sensitivity, strain gauges should be located where maximum induced strains due to the torsion load occur. Since the strain field is averaged over the area covered by the strain gauges, it is very important to determine the loci of the peak strain and ensure the creation of a sufficiently large strain field. FEM is ideally suited to solve this problem.

The sensor body is modeled by solid elements, as shown in Figure 4A. Since the body is symmetrical in geometry and boundary conditions, it suffices to analyze one-half of it, provided that adequate position constraints are imposed on the nodes of the cutting plane. To simplify the FEM, small geometric features of the body are suppressed. Several load cases were investigated, corresponding to axial and shear forces as well as bending and torsion moments.

In our application, the maximum forces and moments are $f_{max} = 1000N$ and $n_{max} = 300Nm$, respectively. A preliminary stress analysis showed that the axial and shear forces have negligible elastic effects because they produce a uniform strain/stress field in the elastic body, resulting in a very weak maximum strain. In fact, the bending moment is the critical nontorsional component, and consequently two different load cases corresponding to the external torsion and bending torques are established for FEM. It is important to note that in robotic applications, the maximum angular deflection due to external torques (which is amplified by the robot links) is a more restrictive constraint than linear deflection due to the forces. It has been investigated that the worst-case strain due to the bending load happens when its axis lies perpendicular to one of the wings, and consequently that axis is chosen for the bending. Moreover, as mentioned earlier, maximum torsional sensitivity requires minimum bending sensitivity. In particular, the radial displacement of the disk's outer diameter due to torsion, principal strain at the strain gauge seats due to both load cases, and maximum von Mises stresses/strains due to a combination of all load cases are selected as the design benchmarks. The described design criteria can be checked with the FEM results to modify the geometry of the sensor iteratively.

In the shape optimization process, we chose as design variables the wing thickness, the distance between two disks, and the inner-hole diameter. The 95 mm outer diameter was selected to match our particular motor. They were varied to maximize the structure efficiency (eq. (6)), which is equivalent to minimizing the performance index

$$\gamma^{-1} \propto \frac{\text{torsional deflection}}{\text{strain due to torsion}},$$

subject to keeping the maximum von Mises stresses within the allowable limits, considering fatigue. The IDEAS solver uses the "Steepest Descent" (the gradient method) method with a penalty function for finding the local minimum—the penalty function simply adds the weighted constraint equation into the objective function.

The postprocessing stage was guided by the following design benchmarks: the tangential and axial displacement of the disk's outer diameter, the principal strain in the axial direction and parallel to the gauge axes due to both load cases, and the maximum von Mises stress/strain due to a combination of all load cases. Hence, the performance index can be obtained from Figures 4C and 4E, while the constraint condition is given by 4B. These design criteria were checked with the FEM results to modify the geometry of the sensor iteratively. The FEM results of the elastic body's final design are shown in Figure 4. The worst-case von Mises stress (i.e., the combination of the two load cases) is shown in Figure 4B, where its maximum occurs at 150 MPa. This is close to the endurance limit of mild steel, with a reasonable factor of safety. Figures 4C and 4D illustrate the tangential and axial displacement fields by which the torsional and bending stiffnesses are carried out—$k_z = 2.7 \times 10^5 \frac{Nm}{rad}$ and $k_x = 4.9 \times 10^6 \frac{Nm}{rad}$, respectively. The axis-symmetric pattern in the figure confirms the correctness of the imposed boundary conditions. Figures 4E and 4F show the strain contour in the axial direction in which the strain gauges are oriented for the first and second load cases, respectively. The FEM results demonstrate that the strain sensitivity in torsion is 7 times higher than in bending, while the bending stiffness is 18 times higher than the torsional stiffness.

4. Calibration and Experiments

The torque sensor is machined from a solid steel rod (Fig. 5). Foil strain gauges (SG-3/350-LY41 from Omega 1995) are cemented at the locations determined by the FEM. The strain gauge bridge is excited by a precisely regulated 8.0 V DC voltage. Instrumentation amplifiers built into the sensor boost the signal level of the Wheatstone bridge output before A/D conversion. We took advantage of the hollow motor shaft, which is common in direct-drive motors, to locate the electronic circuit board beside the sensor. The local signal conditioning provides a stronger output signal and improves the S/N ratio. Moreover, since the electronic circuit is totally enclosed by the motor's hollow shaft, it is well shielded from the powerful magnetic noise created by the motor.
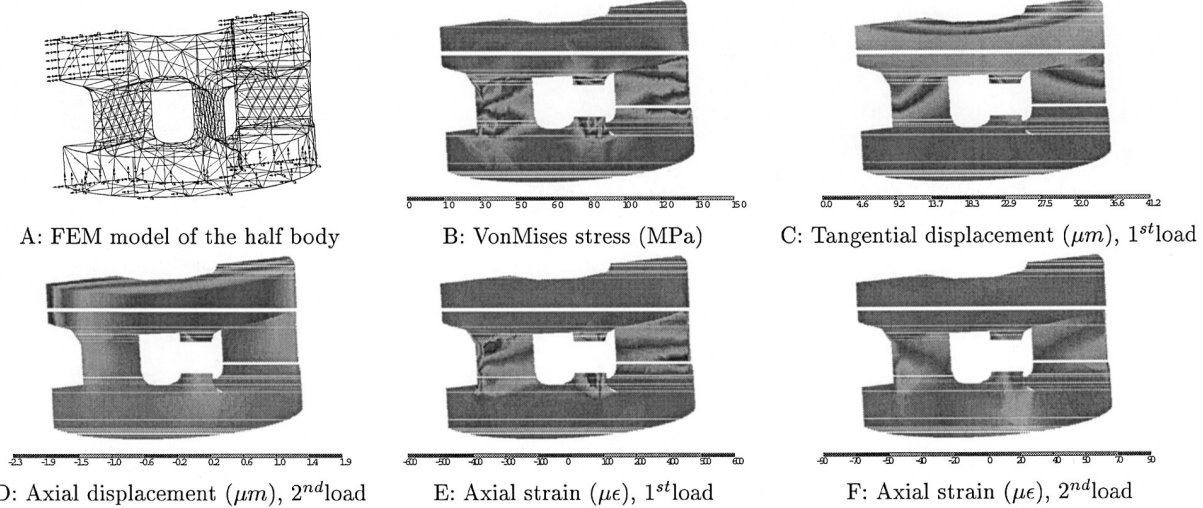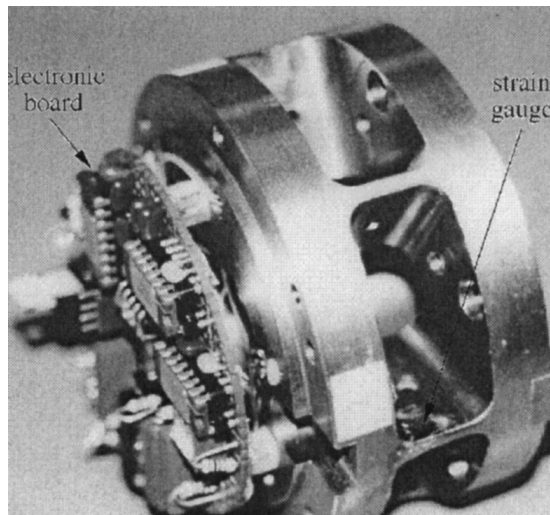
A: FEM model of the half body

B: VonMises stress (MPa)

C: Tangential displacement (μm), 1^{st}load

D: Axial displacement (μm), 2^{nd}load

E: Axial strain ($\mu\epsilon$), 1^{st}load

F: Axial strain ($\mu\epsilon$), 2^{nd}load

Fig. 4. Finite element method analysis.

Fig. 5. The torque sensor prototype.

Fig. 6. The static test setup.

4.1. Static Test

To characterize the linearity and sensitivity of the sensor, static torsional and bending torques are applied in the experimental apparatus illustrated in Figure 6. One side of the sensor is affixed to a bracket, while two aluminum bars are attached radially and axially to the other side. The ends of the bar are connected to a mechanical lever via ropes in which load cells (MLP-50 from Transducer Techniques 1994) are installed. The lever varies the tension in the cord gradually between zero and maximum. During loading and unloading, the reference load cell output and the torque sensor output (device under test) are recorded.

The force transducer signal is scaled to torque and then plotted versus the torque sensor output voltage in Figure 7 for 2000 sample points. The slope of the line indicates the
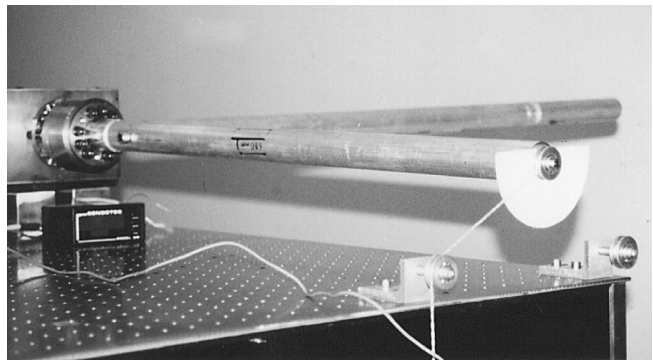
sensor calibration coefficient of $\alpha = 30 \ \frac{mV}{Nm}$. The graph of deviation from linearity is also illustrated in Figure 7. The two trajectories of the error indicate a hysteresis of about 0.1% full scale. The figure shows that all collective deviations from linearity are less than 0.2% full scale.

Low sensitivity to the other axes is one of the key characteristics of a good joint torque sensor. The cross-sensitivity measurements are performed by using the static test bed setup. Forces and moments are applied on different axes by the system of pulleys and weights shown in Figure 6. The bending moment is applied via an axial bar firmly connected to the sensor, while the torsion torque is applied by the radial arm. The direction of the force is set by a pulley, as shown in Figure 6. Theoretically, the sensor output should not be responsive to the bending moment or the forces at all. However, in practice, due to inaccurate placement of the strain gauges and/or differences in the gauge factors of the strain gauges, exact decoupling may not be achieved. In the course of experiment, it becomes evident that, with the exception of the torsion moment, the bending moment dominates the sensitivity of the sensor. The experimental result indicates that the ratio of the
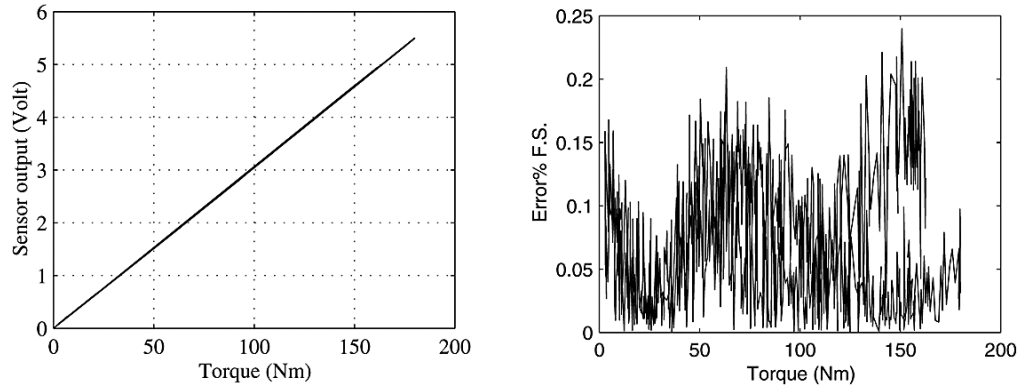
Fig. 7. Sensor output versus applied torque (left) and percent full-scale error from linearity plus hysteresis (right).

sensor readings with respect to the bending and torsion—the cross sensitivity—is only 0.6%. This confirms that the sensor effectively decouples the effect of the nontorsional components on the measured torque signal.

4.2. Dynamic Test

Dynamic testing serves mainly to validate the FEM results on which the stress analysis is based. The experiment is arranged to extract the stiffness of the sensor prototype. Again, the sensor is held rigidly by a bracket while a steel disk is flanged to the other side. The disk is massive, with an inertia of $I_{zz} = 0.24$ kgm^2, and the whole system behaves like a second-order system. To detect all the vibration modes corresponding to all compliance directions, the cross sensitivity is deliberately increased by electrically bypassing the strain of all strain gauge pairs except one. Therefore, the torque sensor no longer has the decoupling property, and its output is the summation of all torque/force components weighted by their corresponding gains. The system is excited impulsively by a hammer, and a data acquisition system records the subsequent vibration with a sampling rate of 3.2 kHz. Figure 8 ("left") shows the impulse response of the system in the time domain, which closely resembles that of a second-order system.

Since the torsion gain is highest, the sensor signal is dominated by torsion vibration, which decays due to the structural damping of the sensor material. Nevertheless, the sensor's modes are shown clearly in the frequency domain. To this end, a 0.5 second interval of the signal is taken via a Hamming window, and then its spectrum is found by FFT. Figure 8 ("right") reveals that the modal frequencies associated with the bending and torsion compliances occur at 150 Hz and 980 Hz. Due to the low damping, the modal frequencies are almost the same as the natural frequencies. The corresponding torsion stiffness can be calculated by $k_z = 4\pi^2 I_{zz}\omega_z^2 = 2.4 \times 10^5 \frac{Nm}{rad}$, which results in a high torsional stiffness. The bending stiffness can be found in the same fashion. However, it should be noted that the relative inertia is half of the inertia for disks (i.e., $I_{xx} = \frac{1}{2}I_{zz}$). The bending stiffness is calculated to be 20

times higher than the torsion stiffness, $k_x = 4.8 \times 10^6 \frac{Nm}{rad}$. A comparison with the FEM predictions reveals an acceptable 20% error.

The viscoelastic effect of the material causes the internal structural damping modeled as viscous friction ζ. Figure 8 ("left") validates the damping model where the exponential envelope corresponding to $\zeta = 0.01$ matches the oscillation decay. The effect of internal viscous friction suggests that the mechanical model of the sensor can be a spring in parallel with a damper. The external torque n_z on the sensor is then equal to

$$n_z = k_z\delta + b_z\dot{\delta},$$

where the viscous coefficient is $b_z = 2\zeta\Omega_z = 9.43\frac{Nm\cdot s}{m}$. The strain gauges deliver a voltage signal as soon as they are exposed to strain. Moreover, since the sensor is calibrated when a static load is applied, the sensor voltage is proportional to the strain (i.e., $v_o \propto \delta$). Therefore, the transfer function from the applied torque to the output voltage is first order:

$$\frac{\text{output}}{\text{input torque}} = \frac{1}{1 + \tau s} \quad \text{where} \quad \tau = \frac{b_z}{k_z},$$

which shows that the viscoelastic property of the sensor's material decreases its bandwidth. Since joint torque feedback is established through a torque sensor, it is imperative to employ a high-bandwidth sensing device (Aghili, Buehler, and Hollerbach 1998a, 2000, 2001). Indeed, the sensor must have a wide bandwidth to ensure that a torque servo system has good sensitivity and fast response. The sensor's cutoff frequency, according to the measured viscous coefficient and the stiffness, is calculated to be 7.6 kHz. This is sufficiently high compared to the bandwidth of typical actuators (e.g., our direct-drive joint) (Aghili, Buehler, and Hollerbach 2000).

5. Conclusion

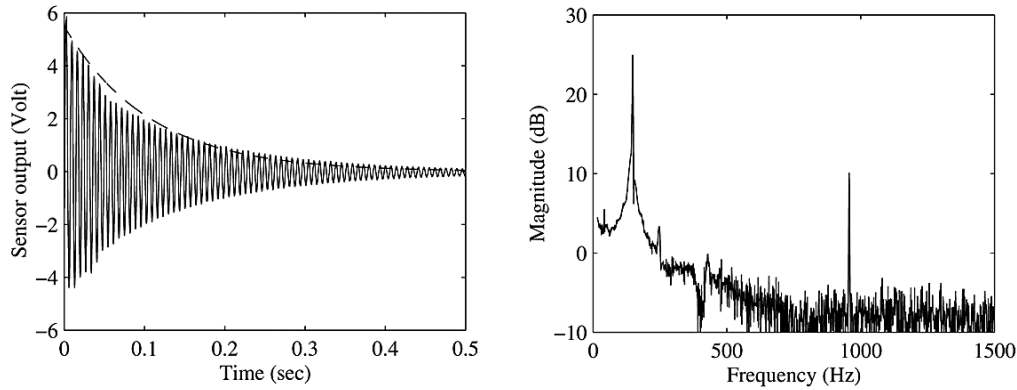Motivated by the need for accurate joint torque sensing in robots, we have designed a new torque sensor, based on the

Fig. 8. Impulse response of the integrated torque sensor with an 0.24 kgm^4 inertia (solid) and the exponential envelope decays according to $\zeta = 0.01$ (dashed) (left). Frequency response of the sensor system (right): experimental data.

Table 1. A Comparison with Various Types of Torque Sensors

Sensor Type	Sensitivity $\frac{mV}{Nm}$	Torsional Stiffness $10^4 \frac{Nm}{rad}$	Bending Stiffness $10^4 \frac{Nm}{rad}$	γ $10^3 \frac{V}{rad}$
B	45.7	3.4	NA	1.55
C	96.5	1.5	NA	1.45
E	30	24	480	7.2

NOTE: NA = not applicable.

hollow hexaform geometry. Its key features are its extremely high stiffness and its insensitivity to the set of support forces and moments that persist in a robot joint. These features permit the mounting of the sensor directly in the joints of a robot manipulator, leading to accurate joint torque sensing and to a compact and modular design. The structure of the sensor also exhibits strain concentration to torsion loads, which maximizes the sensitivity to torsion without sacrificing torsional stiffness. Other design issues such as practical shape consideration, material properties, and overloading have been also considered. The sensor geometry was analyzed and optimized using the FEM. The sensor has been tested extensively to confirm its design goals and is well suited as a torque-sensing device in robots or other industrial high-performance motion control applications.

Finally, to justify the design work presented in this paper, it is imperative to compare the characteristics of our torque sensor with that of conventional commercially available sensors. However, some data (e.g., regarding cross sensitivity and stiffness to bending) are often not available. Nevertheless, for instance, it is known from the elementary strength of material that a cylinder structure is 0.77 times less stiff in bending than in torsion while our sensor is 18 times stronger in bending than in torsion. Our proposed structure also exhibits outstanding torsion characteristics. The torsional sensitivity and stiffness data of type B and type C torque sensors (Fig. 1) were reported in Wu (1985) and Asada and Lim (1985), respectively. A survey of conventional torque sensors shows that our sensor's performance characteristics compare very favorably. A direct quantitative comparison with those types of sensors and type D (i.e., our design) is shown in Table 1.

Acknowledgments

References

Aghili, F., Buehler, M., and Hollerbach, J. M. 1997a. Dynamics and control of direct-drive robots with positive joint torque feedback. *Proceedings of the IEEE International Conference on Robotics and Automation*, April, pp. 1156–1161.

Aghili, F., Buehler, M., and Hollerbach, J. M. 1997b. A joint torque sensor for robots. *ASME International Mechanical Engineering Congress & Exposition*, Dallas, TX, November.

Aghili, F., Buehler, M., and Hollerbach, J. M. 1998a. Disturbance attenuation and load decoupling with h infinity positive joint torque feedback. *Proceedings of the IEEE International Conference on Robotics and Automation*, May, pp. 3613–3618.

Aghili, F., Buehler, M., and Hollerbach, J. M. 1998b. Sensing the torque in a robot's joint. *ASME Mechanical Engineering* 120(9):66–69.

Aghili, F., Buehler, M., and Hollerbach, J. M. 2000. Development of a high performance direct-drive joint. *Proceedings of the IEEE/RSJ International Conference on Intelligent Systems and Robots*, Japan, October, pp. 2151–2158.

Aghili, F., Buehler, M., and Hollerbach, J. M. 2001. Motion control systems with h-infinity positive joint torque feedback. *IEEE Transactions on Control Systems Technology* 9(5):685–695.

AMTI. 1996. *Flange Reaction Torque Sensor*. Technical manual. Scarborough, Ontario: Advanced Mechanical Technology, Inc.

Asada, H., and Lim, S.-K. 1985. Design of joint torque sensors and torque feedback control for direct-drive arms. *ASME Winter Annual Meeting: Robotics and Manufacturing Automation*, PED-vol. 15, Miami Beach, FL, November, pp. 277–284.

Asada, H., and Youcef-Toumi, K. 1987. *Direct-Drive Robots*. Cambridge, MA: MIT Press.

deSilva, C. W., Price, T. E., and Kanade, T. 1987. Torque sensor for direct-drive manipulator. *ASME Journal of Engineering for Industry* 109:122–127.

Hashimoto, M. 1989. Robot motion control based on joint torque sensing. *Proceedings of the IEEE International Conference on Robotics and Automation*, pp. 256–261.

Hashimoto, M., Kiyosawa, Y., and Paul, R. P. 1993. A torque sensing technique for robots with harmonic drives. *IEEE Transactions on Robotics and Automation* 9:108–116.

Himmelstein, S., and Company. 1991. *MCRT Torquemeter*. Technical manual. Hoffman Estates, IL: Himmelstein and Company.

Hirose, S., and Yoneda, K. 1990. Development of optical 6-axial force sensor and its signal calibration considering non-linear interference. *Proceedings of the IEEE International Conference on Robotics and Automation*, Cincinnati, OH, May, pp. 46–53.

Hirzinger, G., et al. 1994. Rotex—the first remotely controlled robot in space. *Proceedings of the IEEE International Conference on Robotics and Automation*, San Diego, CA, May.

Hirzinger, G., et al. 2001. On a new generation of torque controlled light-weight robots. *Proceedings of the IEEE International Conference on Robotics and Automation*, Seoul, Korea, May, pp. 3356–3363.

Jacobsen, S. C., Smith, F. M., Backman, D. K., and Iversen, E. K. 1991. High performance, high dexterity, force reflective teleoperator ii. *ANS Topical Meeting on Robotics and Remote Systems*, Albuquerque, NM, February, pp. 24–27.

Joo, J. W., Lee, H. G., and Kang, D. I. 1998. Design and strain analysis of the hollow cruciform-type torque sensor. *Proceedings of the SEM Spring Conference on Experimental and Applied Mechanics*, Houston, TX, June, pp. 523–525.

Kosuge, K., Takeuchi, H., and Furuta, K. 1990. Motion control of a robot arm using joint torque sensors. *IEEE Transactions on Robotics and Automation* 6(2):258–263.

Lebow. 1997. *Lebow Load Cell Torque Sensor Handbook*. Technical Manual 710. Troy, MI: Eaton Corporation, Lebow Products.

Luh, J.Y.S., Fisher, W. D., and Paul, R.P.C. 1983. Joint torque control by a direct feedback for industrial robot. *IEEE Transactions on Automatic Control* 28:153–161.

Newman, W. S., and Patel, J. J. 1991. Experiments in torque control of the adept-one robot. *Proceedings of the IEEE International Conference Robotics and Automation*, April, pp. 1867–1872.

Omega. 1995. *The Pressure Strain and Force Handbook*. Technical Manual 29. Stamford, CT: Omega.

Pfeffer, L. E., Khatib, O., and Hake, J. 1989. Joint torque sensory feedback in the control of a puma manipulator. *IEEE Transactions on Robotics and Automation* 5(2):418–425.

Shigley, J. E. 1989. *Mechanical Engineering Design*. New York: McGraw-Hill.

Stokic, D., and Vukobratovic, M. 1993. Historical perspectives and state of the art in joint force sensory feedback control of manipulation robots. *Robotica* 11:149–157.

Svinin, M. M., and Uchiyama, M. 1995. Optimal geometric structures of force/torque sensors. *International Journal of Robotics Research* 14(6):560–573.

Tani, Y., Hatamura, Y., and Nagao, T. 1983. Development of small three component dynamometer for cutting force measurement. *Bulletin of the JSME* 26(214).

Transducer Techniques. 1994. *Load Cell Transducer*. Technical manual. Transducer Techniques.

Uchiyama, M., Bayo, E., and Palma-Villalon, E. 1991. A systematic design procedure to minimize a performance index for robot force sensors. *Journal of Dynamic Systems, Measurement, and Control* 113:388–394.

Vischer, D., and Khatib, O. 1990. *Design and Development of Torque-Controlled Joints*. New York: Springer-Verlag.

Vischer, D., and Khatib, O. 1995. Design and development of high-performance torque-controlled joints. *IEEE Transactions on Robotics and Automation* 11:537–544.

Wu, C.-H. 1985. Compliance control of a robot manipulator based on joint torque servo. *International Journal of Robotics Research* 4(3):55–71.

Wu, C.-H., and Paul, R. P. 1980. Manipulator compliance based on joint torque control. *Proceedings of the IEEE International Conference on Decision and Control*, December, pp. 88–94.

Zhang, G., and Furusho, J. 1998. Control of robot arms using joint torque sensors. *IEEE Control Systems* 18(1):48–54.